

375458-2-T

**FINITE ELEMENT-FAST INTEGRAL METHODS FOR
SOLVING SINGLE AND PERIODIC ANTENNA ARRAY
PROBLEMS**

T. Eibert, K. Sertel, D. Filipovich and J. Volakis

Hewlett-Packard Company
1400 Foutaingrove Pkwy
Santa Rosa, CA

375458-2-T = RL-2540

PROJECT INFORMATION

PROJECT TITLE: Algorithms for Phased Array Simulations

REPORT TITLE: Finite element-fast integral methods for solving single and periodic antenna array problems

U-M REPORT No.: 375458-2-T

CONTRACT

START DATE: July 1997

END DATE: May 1999

DATE: February 1998

SPONSOR: David Wilson
Hewlett-Packard EEsof Division
M/S 2US-H
1400 Fountaingrove Pkwy
Santa Rosa, CA 95403-1799

SPONSOR

GRANT/CONTRACT No.: Round Table Agreement Dated 6/01/97

U-M PRINCIPAL

INVESTIGATOR: John L. Volakis
EECS Dept.
University of Michigan
1301 Beal Ave
Ann Arbor, MI 48109-2122
Phone: (313) 764-0500 FAX: (313) 747-2106
volakis@umich.edu
<http://www-personal.engin.umich.edu/~volakis/>

CONTRIBUTORS

TO THIS REPORT: Thomas Eibert, K. Sertel, D. Filipovich and John Volakis

Finite Element - Fast Integral Methods for Solving Single and Periodic Antenna Array Problems

Thomas Eibert, Kubilay Sertel, Dejan S. Filipovich, John L. Volakis

Radiation Laboratory

Department of Electrical Engineering

and Computer Science,

The University of Michigan

Ann Arbor, MI 48109-2212

email volakis@eecs.umich.edu

February 28, 1998

Contents

1	Introduction	4
2	Theory	6
2.1	FE-BI Formulation	6
2.2	Fast Integral Methods	10
3	Adaptive Integral Method	11
3.1	Theory and Implementation	11
3.2	Results: Single Antenna Problem	14
3.3	Results: Periodic Array Antennas	16
4	Fast Multiple Method	18
4.1	Theory and Implementation	18
4.2	Results: Single Antenna Problem	21
4.3	Results: Finite Periodic Arrays	24
5	Conclusion and Future Work	25

Abstract

The introduction of fast integral techniques into the finite element–boundary integral method is investigated in the report. The resulting finite element– fast integral (FE–FI) method permits a reduction of the overall computational requirements of the boundary integral down to $\mathcal{O}(N^\alpha)$ or even down to $\mathcal{O}(N \log(N))$. Coupled with usual $\mathcal{O}(N)$ requirements of the finite element technique, the FE–FI can permit an overall $\mathcal{O}(N \log(N))$ CPU and memory requirement without degradation accuracy or convergence as is the case with truncations based on the absorbing boundary conditions or artificial absorbers.

Here, we consider the application of FE–FI methods for the planar and doubly curved periodic arrays. Both, the fast multiple method (FMM) and adaptive integral method (AIM) are considered.

1 Introduction

Fast integral equation methods were introduced in computational electromagnetics in the early 1990s and have been shown effective in accelerating the computation of matrix-vector products in iterative solvers. The Adaptive Integral Method (AIM) [1] and the Fast Multipole Method (FMM) [2] belong to this class of fast integral solution techniques. Both AIM and FMM reduce the solution time and memory requirement of the moment method solutions.

The application of hybrid finite element (FE) - fast integral (FI) methods to single antennas and infinite periodic antennas (or frequency selective surfaces) is very attractive because it provides full 3D modeling flexibility and exactness in mesh termination. Basically, the finite element method is used to model the dielectric section of the unit cell (or antenna), whereas the boundary integral provides a rigorous mesh truncation. This successful combination is unfortunately limited by the size of the problem, i.e. by the number of the unknowns casted from its discretization (dominant influence comes from the boundary integral part). To alleviate the CPU and memory bottlenecks, acceleration and compression techniques, like AIM and FMM can be used.

FMM achieves its CPU reduction by grouping the far-zone unknowns and interacting their weighted contributions. In the case of AIM, the CPU reduction is achieved by mapping the original moment method (MM) discretization onto a rectangular grid and exploiting the Toeplitz property of the Green's function on this grid. That is, the Fast Fourier Transform (FFT) is invoked to compute the matrix-vector products in the iterative solver. For an arbitrary three dimensional body, a three dimensional FFT is required. For planar radiators, the dimensionality of the FFT is reduced by one, thereby significantly accelerating the computation of the FFT.

In this report, we consider the implementation of AIM and FMM in connection with a finite element-boundary integral solutions for single and periodic antennas and structures. Although our formulation and discussion is on an antenna radiation, it can be easily extended to scattering. Chosen examples and geometries are both, flat and curved, and thus allow us to obtain some general conclusions. The report is organized as follows: In section 2, we review some basic theoretical concepts for array modeling. In chapter 3, we present results based on the AIM implementation. Annular slot cavity backed antennas and infinite periodic array of strip dipoles are used as examples. The FMM theoretical concepts and implementations are examined in chapter 4. Examples computations for cavity backed antennas and arrays mounted on curved surfaces are given showing speed-up using the FMM.

2 Theory

2.1 FE-BI Formulation

The FE-BI formulation for cavity backed antennas recessed in a ground plane is well known and is given in [3, 4, 5]. Bellow we present the corresponding formulation for periodic arrays. The differences are in Green's function, and in the necessity to apply periodic boundary conditions at the volume and surface boundaries to simulate array.

The considered periodic array structure is illustrated in Fig. 1. For time harmonic electromagnetic fields ($e^{j\omega t}$ time convention) the pertinent finite element functional is

$$F(\mathbf{E}, \mathbf{E}_{ad}) = \iiint_V \left[\frac{1}{\mu_r} (\nabla \times \mathbf{E}_{ad}) \cdot (\nabla \times \mathbf{E}) - k_0^2 \mathbf{E} \cdot \mathbf{E}_{ad} + jk_0 Z_0 \mathbf{E}_{ad} \cdot \mathbf{J}^{int} \right] dv + jk_0 Z_0 \iint_S \mathbf{E}_{ad} \cdot (\mathbf{H} \times \hat{n}) ds, \quad (1)$$

where \mathbf{E}_{ad} is the solution of the adjoint field problem, \mathbf{J}^{int} denotes an excitation current within the FE domain, S represents the planar surfaces on the top (and/or bottom) of the FE domain, and \hat{n} is the unit surface normal directed out of the FE domain. Also, k_0 and Z_0 are the free space wave number and wave impedance, respectively. Invoking the surface

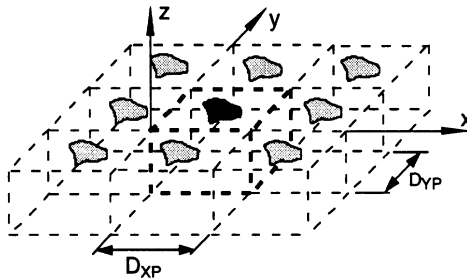


Figure 1: Infinite periodic structure

equivalence theorem, the magnetic field in the surface S of (1) can be expressed as

$$\mathbf{H} = -2j \frac{k_0}{Z_0} \left[\iint_S g(\mathbf{r}, \mathbf{r}') (\mathbf{E} \times \hat{n}) ds + \frac{1}{k_0^2} \nabla \iint_S g(\mathbf{r}, \mathbf{r}') \nabla' \cdot (\mathbf{E} \times \hat{n}) ds \right] + \mathbf{H}^{inc}, \quad (2)$$

where $g(\mathbf{r}, \mathbf{r}')$ is the appropriate periodic Green's function and \mathbf{H}^{inc} is the incident wave. Assuming an array periodic in the xy -plane, with D_{XP} and D_{YP} as the periods in the x - and y -directions, respectively, the periodicity condition for \mathbf{E} in a rectangular lattice is given by

$$\mathbf{E}(x + m D_{XP}, y + n D_{YP}) = \mathbf{E}(x, y) e^{-j\beta_x m D_{XP}} e^{-j\beta_y n D_{YP}}, \quad (3)$$

where

$$\beta_x = k_0 \sin \vartheta_0 \cos \varphi_0, \quad \beta_y = k_0 \sin \vartheta_0 \sin \varphi_0 \quad (4)$$

and (ϑ_0, φ_0) are the chosen scan directions of the array. Using the periodicity condition and the boundary integral representation (2), the computational domain can be reduced to a single unit cell of the array. In the implementation of the hybrid FE-BI method, this requires the imposition of appropriate phase boundary conditions in the FE and in the BI portions of the method. Moreover, in (2) $g(\mathbf{r}, \mathbf{r}')$ must be replaced by the Green's function for an infinite array of δ -sources. In our implementation, the infinite series representation of periodic Green's function is calculated using Ewald's transform which subdivides series into spatial and spectral domain components in a manner that optimal convergence is achieved. To construct a linear set of equations from (1) and (2), we must first tessellate the volume and introduce expansions for each of the tessellation elements. For this application, the chosen tessellation elements can be of constant depth but must be more adaptable for surface modeling. The edge-based prismatic elements presented in [4, 5] allow for this type of flexibility.

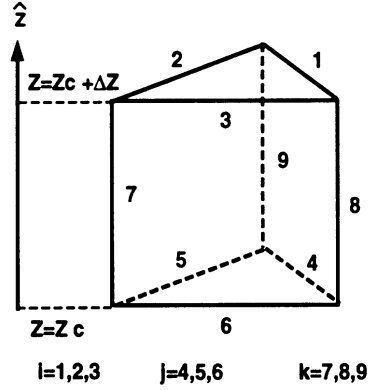


Figure 2: Right angled prism

Using the same type of tessellation elements (see Figure 2), the field is expanded within the cavity volume as

$$\mathbf{E}^e = \sum_{j=1}^9 E_j^e \mathbf{W}_j^e = [\mathbf{W}]_e^T \{E^e\} \quad (5)$$

where $[\mathbf{W}]_e = [\{W_x\}, \{W_y\}, \{W_z\}]$ and $\{E^e\} = \{E_1^e, E_2^e, \dots, E_9^e\}^T$ are specified explicitly in [5]. On the aperture, since the top and bottom faces of the prism are triangles, these are reduced to

$$\mathbf{E}^s(\mathbf{r}) = \sum_{i=1}^3 E_i^s \mathbf{S}_i^s(\mathbf{r}) = [S]_s^T \{E^s\} \quad (6)$$

where $[S]_s = [S_x, S_y]$ and

$$\mathbf{S}_i = \frac{l_i}{2A^e} \hat{z} \times (\mathbf{r} - \mathbf{r}_i) \quad (7)$$

To generate a linear system for E_j^e , (5) and (6) are substituted into (1) and (2) and

Galerkin's method (setting $\mathbf{T} = \mathbf{W}$) is employed to yield the assembled system

$$[\mathcal{A}] \begin{Bmatrix} \{E^V\} \\ \{E^S\} \end{Bmatrix} + \begin{bmatrix} [0] & [0] \\ [0] & [\mathcal{B}] \end{bmatrix} \begin{Bmatrix} \{E^V\} \\ \{E^S\} \end{Bmatrix} = \begin{Bmatrix} \{b^V\} \\ \{b^S\} \end{Bmatrix}. \quad (8)$$

In this system, $\{E^V\}$ denotes the field unknowns within the volume enclosed by S_o , whereas $\{E^S\}$ represents the corresponding unknowns on the boundary S_o . The excitation column $\{b^V\}$ are due to internal antenna sources and $\{b^S\}$ is associated with the incident field excitations (for scattering).

2.2 Fast Integral Methods

The FE-BI system (8) is partly sparse and partly dense. More specifically $[\mathcal{A}]$ is sparse, whereas $[\mathcal{B}]$ is dense. Thus, although $[\mathcal{B}]$ is much smaller in rank than $[\mathcal{A}]$, it is usually responsible for most of the CPU and memory when an iterative algorithm is used for the solution of (8). To alleviate the CPU and memory requirements, fast integral methods have recently been introduced [1, 2, 9, 10] to perform the matrix-vector product $[\mathcal{B}]\{E^S\}$ much faster and with much less memory. Two of these approaches are the adaptive integral method (AIM) [1], and the fast multipole method (FMM) [2, 10]. Both FMM and AIM reduce the CPU time and memory requirement from $O(N^2)$ down to $O(N^\alpha)$ where $\alpha \leq 1.5$. The main feature of AIM and FMM is the decomposition of the matrix as

$$[\mathcal{B}] = [\mathcal{B}]^{near} + [\mathcal{B}]^{far} \quad (9)$$

based on some threshold distance referred to as the near-zone radius. The matrix $[\mathcal{B}]^{near}$ contains the interactions between elements separated less than the threshold distance, whereas $[\mathcal{B}]^{far}$ contains the remaining interactions. The elements of $[\mathcal{B}]^{near}$ are evaluated without approximation. However, the product $[\mathcal{B}]^{far} E^S$ is evaluated in an approximate manner leading to a much faster execution.

Next, we describe how the evaluation of $[\mathcal{B}]^{far}\{E^S\}$ is performed for each of the fast algorithms.

3 Adaptive Integral Method

3.1 Theory and Implementation

The basic idea of AIM is to split $[Z]$ (equivalent to $[\mathcal{B}]$ in (9) as

$$[Z] = [Z^{near}] + [Z^{far}], \quad (10)$$

where $[Z^{near}]$ contains the elements of $[Z]$ that are near the self-cell and correspondingly $[Z^{far}]$ contains the remaining "far-zone" elements of $[Z]$. AIM reduces the CPU time and memory of the iterative solver by exploiting convolutional properties of the Green's function for the evaluation of the matrix-vector products associated with the mostly full matrix $[Z^{far}]$ [1]. That is, the far-zone matrices are not explicitly generated and the matrix-vector products are performed in the discrete Fourier domain (DFT) utilizing appropriate 2D FFT algorithms [18]. However, the convolutional properties can only be exploited on a regular grid and therefore, the basis functions on the original and possibly irregular triangular mesh must first be mapped onto a regular grid. To do so, we introduce auxiliary basis functions on a regular rectangular grid which is coincident with the original triangular grid [19]. The auxiliary expansion for the magnetic surface currents is given by

$$\mathbf{M}_s^{aux} = \sum_{m=1}^M \sum_{n=1}^N [M_{mn}^x \hat{x} + M_{mn}^y \hat{y}] \delta(x - x_0 - m\Delta x) \delta(y - y_0 - n\Delta y), \quad (11)$$

where (x_0, y_0) is the lower left corner of the regular grid and $\Delta x, \Delta y$ are the sample distances in the x and y directions, respectively. Since we work with a mixed potential integral equation (MPIE) formulation for the BI implementation, we must introduce an additional expansion for the divergence of the magnetic surface currents,

$$\nabla \cdot \mathbf{M}_s^{aux} = \sum_{m=1}^M \sum_{n=1}^N q_{mn} \delta(x - x_0 - m\Delta x) \delta(y - y_0 - n\Delta y) \quad (12)$$

In mapping the original basis functions onto the regular grid we relate each basis function to the auxiliary δ -basis functions on the nine closest grid points of the regular grid. This is done by equating a sufficiently large number of the corresponding moments of basis functions from the two coincident grids. All moments can be evaluated analytically or numerically, and for each basis function of the original mesh, three linear algebraic systems of order 9 must be evaluated. This leads to the construction of the sparse mapping matrices $[\Lambda]_x$, $[\Lambda]_y$, and $[\Lambda]_q$ with n_s rows and nine columns. The Z matrices for the rectangular grid can be expressed as

$$[Z]_{AIM}^{total} = [\Lambda]_x[G][\Lambda]_x^T + [\Lambda]_y[G][\Lambda]_y^T + [\Lambda]_q[G][\Lambda]_q^T. \quad (13)$$

Here, $[G]$ is a Toeplitz matrix whose elements stem from the periodic Green's function evaluated on the grid points of the regular grid. For the implementation of AIM it is assumed that $[Z]_{AIM}^{total}$ is sufficiently accurate for the far zone elements. For the near zone interactions we keep original matrix elements. Therefore, we decompose the AIM matrices as

$$[Z]_{AIM}^{total} = [Z]_{AIM}^{near} + [Z]_{AIM}^{far} \quad (14)$$

and when this is combined with (10), we can rewrite the original Z matrices as

$$[Z]^{approx} = ([Z]^{near} - [Z]_{AIM}^{near}) + [Z]_{AIM}^{total}. \quad (15)$$

With this representation of $[Z]$, the near zone interactions are evaluated without compromise in accuracy. However, since the majority of $[Z]^{approx}$ consists of the Toeplitz kernel $[G]$, the associated matrix-vector products can be performed using only $\mathcal{O}(n_s)$ memory and $\mathcal{O}(n_s \log n_s)$ CPU time. In the final numerical implementation, a near-zone threshold is defined so that $[Z]^{approx}$ is sufficiently accurate representation of $[Z]$. The threshold distance is controlled by the quasi-static singularities of the Green's function. In the case of the

infinite periodic Green's function, we must also account for singularities associated with those elements which neighbor the boundaries of the unit cell since the latter are adjacent to the next periodic cell.

For calculation of matrix-vector products in an iterative solver, $[Z]_{AIM}^{far}$ is not computed explicitly. After mapping the actual source distributions onto the regular grid through Λ matrices, the pertinent matrix-vector products are performed in DFT domain using FFT algorithm for the corresponding transformation. After transformation of the results back to the spatial domain, the fields on the original mesh are obtained by reverse mapping between the auxiliary unknowns and the original grid unknowns. However, for a computation of $[Z]_{AIM}^{near}$, it is advantageous to collect contributions of the regular grid in the spatial domain before the Toeplitz Green's function is transformed into the DFT domain.

3.2 Results: Single Antenna Problem

We analyzed the planar cavity backed annular slot antenna with one, two, four and twelve elements. To increase the BI unknowns, we considered bistatic scattering from the complementary structures (annular strips) obtained by inverting metallic and dielectric part of the antenna aperture.

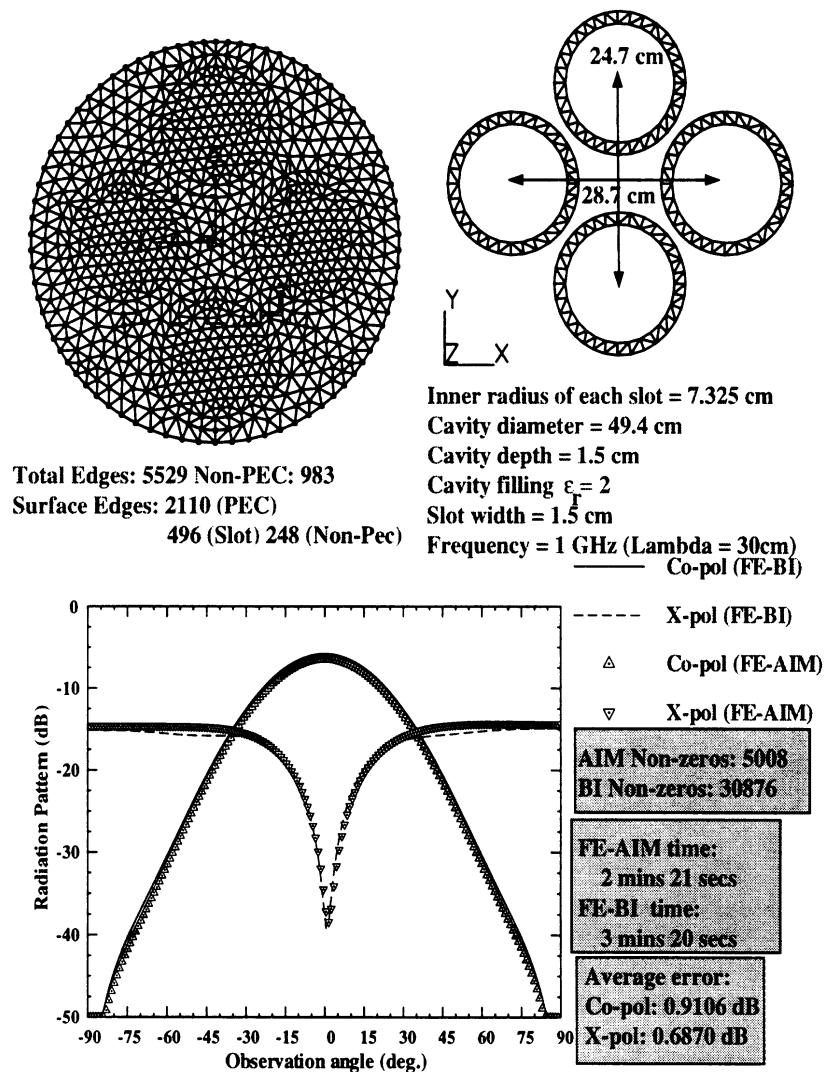


Figure 3: Geometry, parameters and radiation pattern ($\phi = 90^\circ$) for cavity backed 4-elements annular ring slot antenna

These scatterers may not have practical importance, but are nevertheless quite appropriate for the case studies of interest. The aperture surface was discretized in a nonuniform triangle mesh using SDRC I-DEAS. The radiation pattern, aperture discretization and parameters for a 4 element annular slot array are given in Fig. 3, with corresponding memory requirements and CPU time (per iteration) given in Fig. 4. Clearly, large memory savings are attained by AIM. We should also point out that the problem 12 annular strips with 5695 surface unknowns, required 360MBytes and could not be therefore executed on a typical workstation. AIM required only 95MBytes in addition to the CPU reduction.

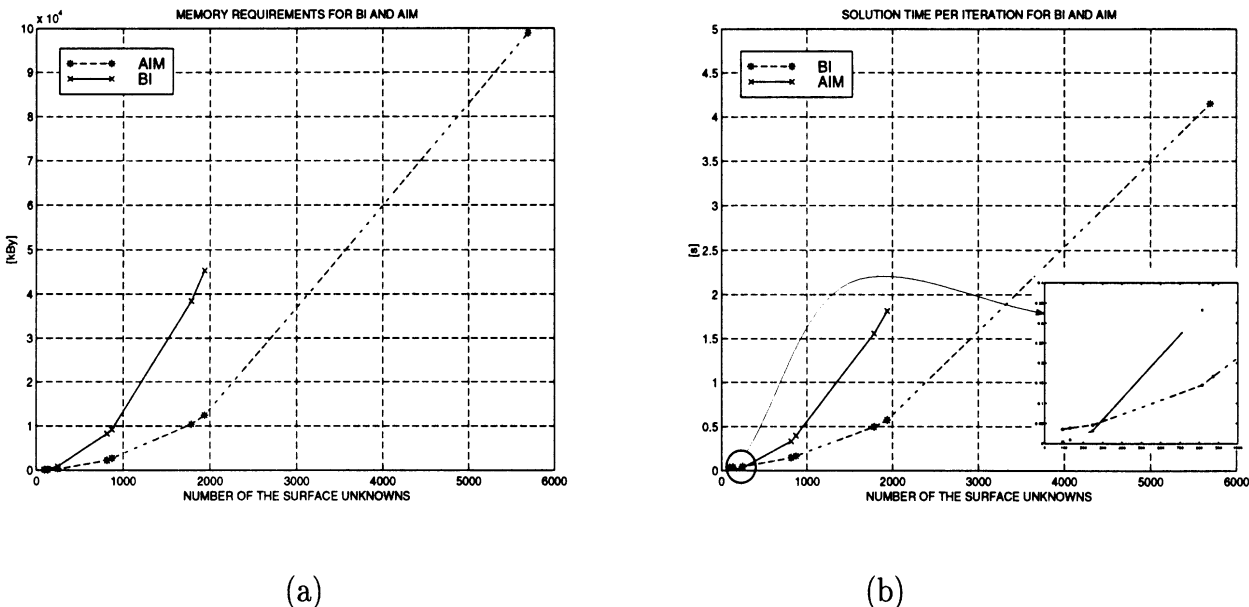


Figure 4: (a) Comparison of the memory requirements, (b) Comparison of the CPU time consumed per one iteration.

3.3 Results: Periodic Array Antennas

To show the speed improvements and storage reduction due to AIM, we consider a relatively simple strip dipole frequency selective surface (FSS) as shown in Fig. 5 (see also [17]). We calculated the reflection coefficient for three different FE meshes as described in Table 1 using triangular surface meshes for discretizing the planar surface of the unit cell (right-angled prisms were used in the volume). The BI was applied on the top and bottom of the cell for mesh truncation, resulting in two fully populated BI submatrices.

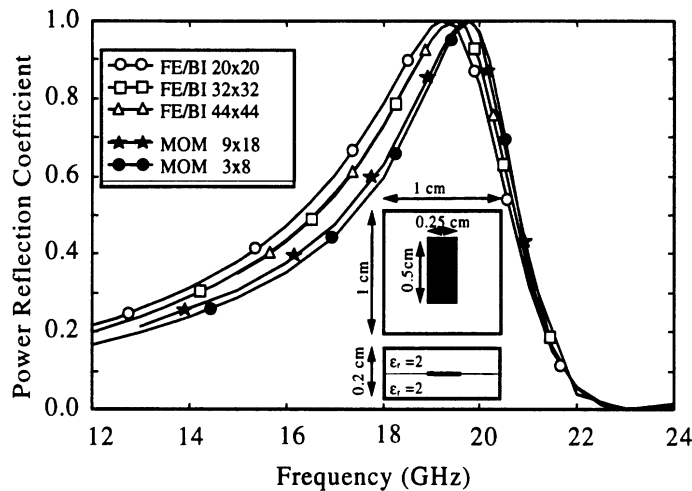


Figure 5: Resonance curves for strip dipole FSS

Since BI matrices were identical, only one matrix was computed. Table 1 shows model parameters and the size of the system matrices with and without AIM for BI matrix computations. The number of matrix elements, (columns 5 and 6 of this table), comprise both, the top and bottom BI matrices. As noted earlier, the AIM implementation requires that only near-elements of the BI matrices be calculated explicitly. This results in memory savings of up to a factor of 15 for model 3 and these savings will increase further for surface meshes with a larger number of unknowns. The CPU times for different models are summarized

in Table 2. The FE matrix fill time is, of course, the same for AIM and the conventional implementation of the hybrid method.

Model	Surf. mesh	Surf. unk.	Vol. unk.	Matrix elements	
				AIM	Conv.
1	20×20	2*1240	7435	588 079	3 000 000
2	32×32	2*3136	35432	2 183 120	20 000 000
3	44×44	2*5896	67000	4 672 610	71 000 000

Table 1: Unknowns and storage for different discretization models

Mod.	FE fill	BI fill		Solver		Iterations		Total	
		AIM	Conv.	AIM	Conv.	AIM	Conv.	AIM	Conv.
1	3	736	1 400	228	166	227	234	967	1 569
2	38	1 930	7 330	1 081	1 446	415	364	3 049	8 814
3	70	3 821		5 073		676		8 964	

Table 2: CPU times (in sec) for the different discretization models

For the investigated problem the largest CPU savings were obtained due to the reduced BI matrix fill time. For small BI subsystems (as is the case with model1), AIM did not result in CPU speed-ups. However, for larger BI subsystems, the lower complexity of AIM resulted in considerable CPU reduction (see model 2). For model 3, we performed only calculations based on AIM since the storage requirements were 850 MByte using traditional implementation. AIM reduced storage down to 70 MBytes.

4 Fast Multiple Method

4.1 Theory and Implementation

The FMM [2, 9, 10] is based on two elementary identities. One of them is the expansion [8] of the scalar Green's function appearing in moment matrix elements as

$$\frac{e^{ik|\mathbf{r}+\mathbf{d}|}}{|\mathbf{r}+\mathbf{d}|} = ik \sum_{l=0}^{\infty} (-1)^l (2l+1) j_l(kd) h_l^{(1)}(kr) P_l(\hat{\mathbf{d}} \cdot \hat{\mathbf{r}}). \quad (16)$$

Here j_l is the spherical Bessel function, $h_l^{(1)}$ is the spherical Hankel function of the first kind, P_l is the Legendre polynomial, and $d < r$ is the condition for the valid of the expansion. In the FMM formulations, where the source point is denoted by \mathbf{x}' and the observation point by \mathbf{x} , \mathbf{r} will be chosen to be close to $\mathbf{x} - \mathbf{x}'$ so that \mathbf{d} will be small as depicted in Fig. 6. The second identity is the expansion of the product $j_l P_l$ appearing in Eq. (16) as a sum of propagating plane waves (spectral integral):

$$4\pi i^l j_l(kd) P_l(\hat{\mathbf{d}} \cdot \hat{\mathbf{r}}) = \int d^2 \hat{\mathbf{k}} e^{i\mathbf{k} \cdot \mathbf{d}} P_l(\hat{\mathbf{k}} \cdot \hat{\mathbf{r}}). \quad (17)$$

Using this identity, the expansion (16) can be rewritten as

$$\frac{e^{ik|\mathbf{r}+\mathbf{d}|}}{|\mathbf{r}+\mathbf{d}|} = \frac{ik}{4\pi} \int d^2 \hat{\mathbf{k}} e^{i\mathbf{k} \cdot \mathbf{d}} \sum_{l=0}^{\infty} (2l+1) h_l^{(1)}(kr) P_l(\hat{\mathbf{k}} \cdot \hat{\mathbf{r}}), \quad (18)$$

where the orders of summation and integration are interchanged. The speed-up of FMM is derived from the observation that the sum

$$T_L(kr, \hat{\mathbf{k}} \cdot \hat{\mathbf{r}}) = \sum_{l=0}^L (2l+1) h_l^{(1)}(kr) P_l(\hat{\mathbf{k}} \cdot \hat{\mathbf{r}}) \quad (19)$$

is independent of kd and can thus be computed for various values of kr which can be reused in the computation of the Green's function. The number of terms, $L+1$, kept for approximating the sum depends on the maximum value of kd , and the desired accuracy.

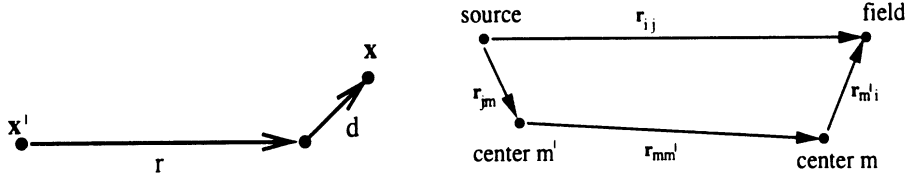


Figure 6: The geometry constructions used in FMM formulations, illustrating the relation between source point, field point and the group centers.

Noting that the direct path from the source to the field point can be decomposed into three parts (see Fig. 6) where

$$\mathbf{r}_{ji} = \mathbf{r}_{jm} + \mathbf{r}_{mm'} - \mathbf{r}_{im'}, \quad (20)$$

the Green's function can be rewritten as

$$\begin{aligned} 4\pi\bar{\mathbf{G}}(\mathbf{r}_j, \mathbf{r}_i) &= \left[\bar{\mathbf{I}} - \frac{1}{k^2} \nabla \nabla' \right] \frac{e^{ikr_{ji}}}{r_{ji}} \\ &\approx \int d^2\hat{k} \left[\bar{\mathbf{I}} - \frac{1}{k^2} \nabla \nabla' \right] e^{i\mathbf{k} \cdot (\mathbf{r}_{jm} - \mathbf{r}_{im'})} T_L(kr_{mm'}, \hat{k} \cdot \hat{r}_{mm'}) \\ &= \int d^2\hat{k} \left[\bar{\mathbf{I}} - \hat{k}\hat{k} \right] e^{i\mathbf{k} \cdot (\mathbf{r}_{jm} - \mathbf{r}_{im'})} T_L(kr_{mm'}, \hat{k} \cdot \hat{r}_{mm'}). \end{aligned} \quad (21)$$

The matrix entries can then be approximated as

$$\begin{aligned} B_{ij} &= 2 \int_S ds \tilde{\mathbf{S}}_i(\mathbf{r}) \cdot \int_{s'} ds' \left[\tilde{\mathbf{S}}_j(\mathbf{r}') + \frac{1}{k^2} \nabla' \cdot \tilde{\mathbf{S}}_j(\mathbf{r}') \nabla \right] \frac{e^{ikR}}{R} \\ &\approx \frac{ik}{2\pi} \int d^2\hat{k} \mathbf{V}_{fmj}(\hat{k}) \cdot T_L(kr_{mm'}, \hat{k} \cdot \hat{r}_{mm'}) \mathbf{V}_{sm'i}^*(\hat{k}), \end{aligned} \quad (22)$$

with

$$\begin{aligned} \mathbf{V}_{sm'i}(\hat{k}) &= \int_S ds' e^{i\mathbf{k} \cdot \mathbf{r}_{im'}} \left[\bar{\mathbf{I}} - \hat{k}\hat{k} \right] \cdot \tilde{\mathbf{S}}_i(\mathbf{r}_{im'}), \\ \mathbf{V}_{fmj}(\hat{k}) &= \int_S ds e^{i\mathbf{k} \cdot \mathbf{r}_{jm}} \left[\bar{\mathbf{I}} - \hat{k}\hat{k} \right] \cdot \tilde{\mathbf{S}}_j(\mathbf{r}_{jm}) \end{aligned} \quad (23)$$

in which $\tilde{\mathbf{S}}_i$ and $\tilde{\mathbf{S}}_j$ denote the expansion and testing functions for the unknown magnetic surface current density. For our computations, we used the well known RWG [6] basis functions. Note also that $*$ denotes complex conjugation.

To realize the FMM speed-up the computational domain is divided into M groups. The total memory storage needed is $O(N^2/M) + O(KN) + O(KLM^2)$ where K is the number of wave vector directions used in the numerical evaluation of the outermost integral in Eq. (22). Using the proportionalities $K \propto L^2$, $D^2 \propto N/M$, and $L \propto D$, this expression can be simplified to $C_1(N^2/M) + C_2(NM\sqrt{N/M})$, where C_1 and C_2 are machine (and implementation) dependent constants. The coefficient C_2 is actually quite small compared to C_1 and thus the memory is dominated by the $O(N^2/M)$ term.

The CPU requirement of this FMM implementation is $O(NM) + O(N^2/M)$ [9, 10]. This can be minimized by choosing $M = \sqrt{N}$ and the result is an $O(N^{1.5})$ algorithm. The memory required for the FMM also becomes $O(N^{1.5})$. In practice, both the operation cost and the memory requirement of FMM is less than those of standard MoM formulation for problem sizes larger than 1000, making the FMM more suitable for the solution of large problems.

4.2 Results: Single Antenna Problem

One concern with the approximations introduced by FMM is accuracy for antenna simulations. Thus for validation we first apply FMM for the analysis of a 3.5cm.×3.5cm. cavity-backed patch mounted on a cylindrical surface of radius 14.95cm. The patch is placed on the aperture of a cavity 0.3175cm. deep filled with a dielectric layer having $\epsilon_r=2.32$. Fig. 7 shows the layout of the curved antenna obtained by wrapping the flat antenna on the cylindrical surface and corresponds to the one considered in [7]. As explained in [7], two different radiation modes (axial and circumferential) exist depending on the feed location. The radiation patterns for the axial and circumferential excitation modes are shown in Fig. 8(a). As expected, the FMM calculations are in agreement with measurements in the broadside region. Toward the shadow directions (around $\theta=-90^\circ$ and $\theta=90^\circ$), the agreement deteriorates since we used the half-space Green's function where in [7] the exact cylindrical Green's function was employed. In the region $60 \leq \theta \leq -60$ the measured and calculated patterns agree to within 1 dB. The input impedance dependence on antennas curvature is plotted in Fig. 8(b) for the circumferentially polarized patch. The results are again in good agreement with those presented in [7] and the resonant frequency can be accurately predicted since it is a more local phenomenon. Figures 9(a) and (b) show the comparison of the timings for the conventional FE-BI method with and without FMM. The speed up of FMM is observed for all problem sizes of practical interest. Fig. 9(a) depicts the trend for the total solution time and Fig. 9(b) shows the time consumed per iteration in the iterative solver. In essence, Fig. 9(a) includes the matrix fill time, where Fig. 9(b) does not. Clearly, for small number of BI unknowns (less than 2000), the CPU time speed-up is primarily due to the faster matrix fill. We can conclude that the FMM implementation is both robust and requires much

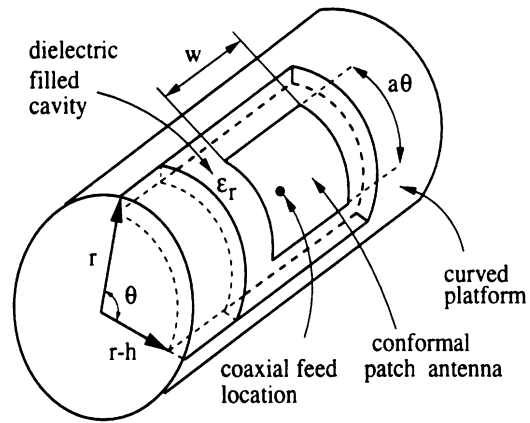


Figure 7: Microstrip patch antenna on a curved platform.

less resources for large scale implementations. We are currently investigating more accurate methods applicable to arbitrarily curved antenna geometries.

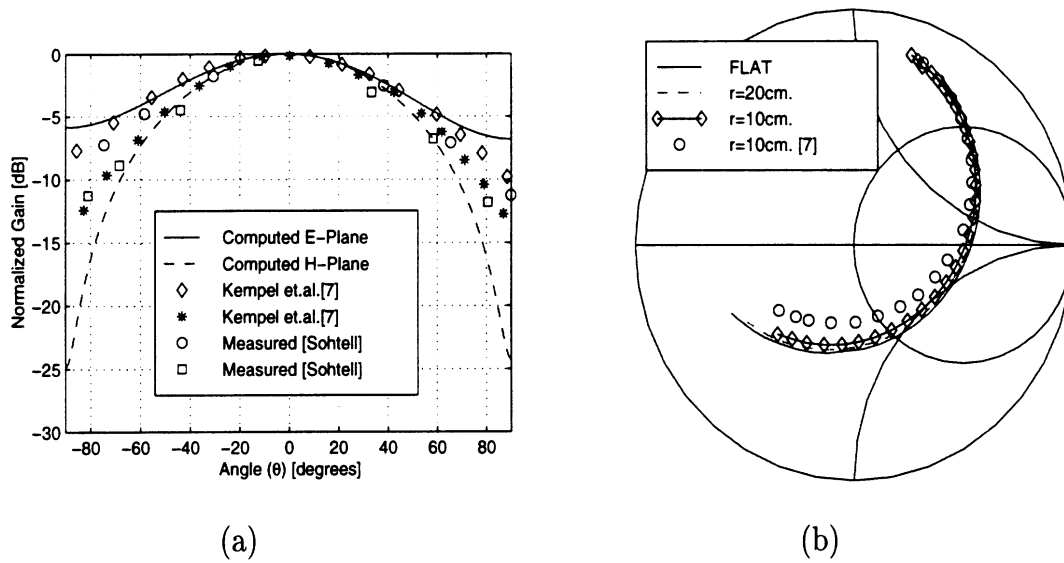


Figure 8: (a) The radiation pattern of the curved antenna, (b) The input impedance for the circumferentially polarized antenna.

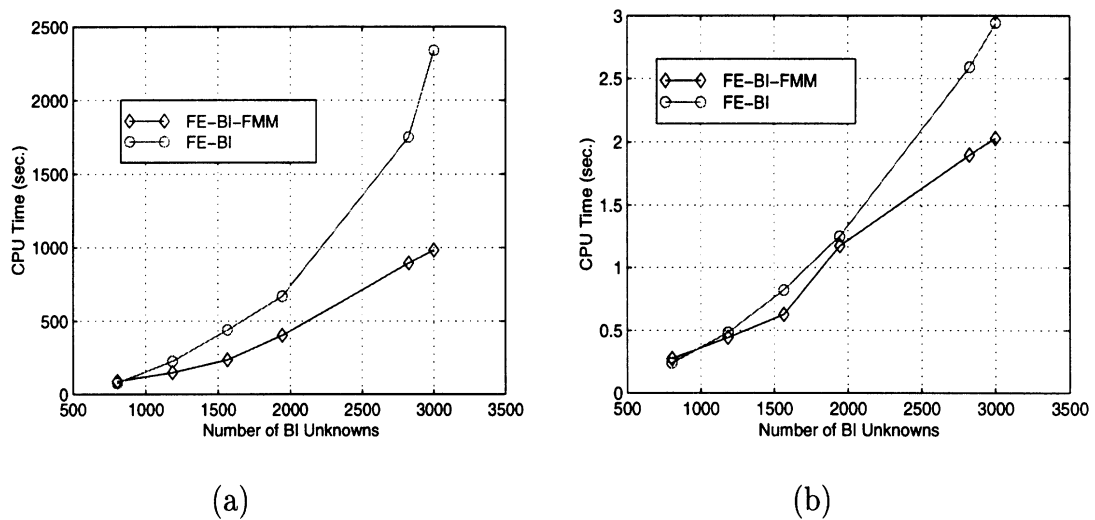


Figure 9: (a) Comparison of the total CPU time consumed for the solution, (b) Comparison of the CPU time consumed per iteration.

4.3 Results: Finite Periodic Arrays

The greatest advantage of the FMM implementation is its capability for an efficient computation of 3D problems. The necessity of using 3D-FFT's in AIM implementations may not render AIM as attractive without suitable optimizations on the implementation of the FFT. Thus, for doubly curved arrays we consider implementation of the FE-FI methods with FMM rather than AIM. Below, we show some results for the analysis of printed dipole array on a curved surface. The radiation pattern for such an array is shown in Fig. 10. These are the preliminary results.

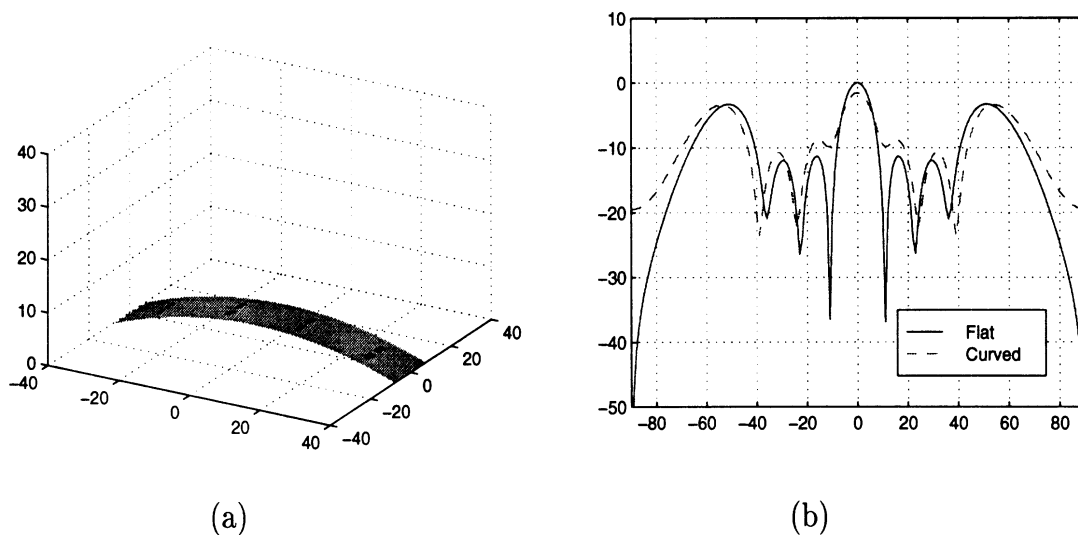


Figure 10: (a) Curved array geometry, (b) Radiation patterns for flat and curved arrays.

At this point, we simply present a comparison between the calculations for the flat and curved arrays. As expected, the two patterns agree near broadside and deviate only near endfire grazing. The curved array does not have a null at $\theta=90^\circ$ and -90° since the array continues to radiate in the shadow region of the cylindrical surface.

5 Conclusion and Future Work

Hybrid FE-BI method is indeed a powerful and flexible approach for EM analysis. Use of fast integral methods such as AIM and/or FMM can considerably decrease CPU time and reduce memory. Both, AIM and FMM accelerate and compress the solution requirements thus overcoming the usual bottlenecks in considering large scale problems. The most attractive feature of FI methods is that speed-up and memory reduction are obtained irrespective of the machine or computational platform. Efficient programming and parallelization will only provide further speed-ups and more efficient use of resources.

For planar geometries AIM is certainly preferred since it naturally provides an $\mathcal{O}(N \log(N))$ CPU requirements as is the case with CG-FFT. Implementations of the FMM is however easier to implement for curved arrays.

To better address the speed-up and efficiency of the FMM and AIM in the future we will:

1. Examine more optimal implementation of the AIM algorithm (for planar antenna geometries);
2. Complete FMM formulation and validation for arbitrary 3D geometries;
3. Investigate applicability of AIM (and FMM) in domain decomposition for more general applications.

References

- [1] E. Bleszynski, M. Bleszynski, and T. Jaroszewicz, "AIM: Adaptive Integral Method for Solving Large-Scale Electromagnetic Scattering and Radiation Problems" *Radio Science*, pp. 1225-1251, Sep.-Oct. 1996
- [2] R. Coifman, V. Rokhlin, and S. Wandzura, "The Fast Multipole Method for the Wave Equation: A Pedestrian Prescription", *IEEE Antennas and Propagation Magazine*, Vol. 35, pp. 7-12, June 1993
- [3] J.L. Volakis, T. Özdemir and J. Gong "Hybrid Finite Element Methodologies for Antennas and Scattering", *IEEE Trans. Antenna Propagat.*, pp. 493-507, March 1997
- [4] J.Gong, J.L. Volakis and H.T.G. Wang, "Efficient Finite Element Simulation of Slot Antennas Using Prismatic Elements", *Radio Sci.*, Vol. 31, No. 6, pp. 1837-1844, Nov-Dec. 1996
- [5] T. Özdemir and J. L. Volakis, "Triangular Prisms for Edge-Based Vector Finite Elements Analysis" *IEEE Trans. Antennas Propagat.*, pp. 788-797, May 1997
- [6] S. M. Rao, D. R. Wilton, and A. W. Glisson, "Electromagnetic Scattering by Surfaces of Arbitrary Shape", *IEEE Trans. Antennas Propagat.*, pp. 409-418, May 1982
- [7] L. C. Kempel, J.L. Volakis and R. J. Silva, "Radiation by Cavity-Backed Antennas on a Circular Cylinder", *IEE Proc.-Microw. Antennas Propag.*, Vol. 142, No. 3, pp. 233-239, June 1995
- [8] M. Abramowitz and I. A. Stegun, "Handbook of Mathematical Functions", National Bureau of Standards, 1972

- [9] W. C. Chew, J. Jin, C. Lu, E. Michielssen, and J. M. Song, "Fast Solution Methods in Electromagnetics", *IEEE Trans. Antenna Propagat.*, Vol. 45, No. 3, pp. 533-543, March 1997
- [10] S. S. Bindiganavale and J.L. Volakis, "Comparison of Three FMM Techniques for Solving Hybrid FE-BI Systems", *IEEE Antennas and Propagation Magazine*, Vol. 39, No. 4, pp. 47-59, August 1993
- [11] E. W. Lucas, T. W. Fontana, A 3-D Hybrid Finite Element/Boundary Element Method for the Unified Radiation and Scattering Analysis of General Infinite Periodic Arrays, *IEEE Trans. AP*, Vol. 43, No. 2, pp. 145-153, Feb. 1995.
- [12] D. T. McGrath, V. P. Pyati, Periodic Structure Analysis Using a Hybrid Finite Element Method, *Radio Science*, Vol. 31, No. 5, pp. 1173-1179, Sep/Oct. 1996.
- [13] J. C. Vardaxoglou, A. Hossainzadeh, A. Stylianou, Scattering from Two-Layer FSS with Dissimilar Lattice Geometries, *IEE Proc. H*, Vol. 140, No. 1, pp. 59-61, Feb. 1993.
- [14] H. Aroudaki, V. Hansen, H.-P. Gemünd, E. Kreysa, Analysis of Low-Pass Filters Consisting of Multiple Stacked FSS's of Different Periodicities with Applications in the Submillimeter Radioastronomy, *IEEE Trans. AP*, Vol. 43, No. 12, pp. 1486-1491, Dec. 1995.
- [15] H.-Y. D. Yang, R. Diaz, N. G. Alexopoulos, Reflection and Transmission of Waves from Multilayer Structures with Planar Implanted Periodic Material Blocks, *J. of the Opt. Soc. of Am., B*, Oct. 97.
- [16] E. Bleszynski, M. Bleszynski, T. Jaroszewicz, *Radio Science*, Vol. 31, No. 5, pp. 1225-1251, Sep./Oct. 1996.

- [17] R. Mittra, C. H. Chan, T. Cwik, *Proc. IEEE*, Vol. 76, No. 12, pp. 1593–1615, Dec. 1988.
- [18] J. L. Volakis and K. Barkeshli, *Appl. of It. Meth. to Electromag. and Signal Proc.*, ed. T. Sarkar, Elsevier Pub. Co., pp. 159-240, 1991.
- [19] J. Gong, J. L. Volakis, A. Woo and H. Wang, *IEEE Trans. AP*, Vol. 42, No. 9, pp. 1233-1242, Sept. 1994.